Absorption-spectroscopy diagnosis of pusher conditions in laser-driven implosions

A. Hauer and R. D. Cowan
Los Alamos National Laboratory, University of California, Los Alamos, New Mexico 87545

B. Yaakobi, O. Barnouin, and R. Epstein
Laboratory for Laser Energetics, College of Engineering and Applied Science, University of Rochester, 250 East River Road, Rochester, New York 14623-1299
(Received 28 October 1985)

Absorption spectroscopy has been used in this work to diagnose the conditions in the pusher of laser-imploded targets. Absorption lines are produced when continuum radiation from the hot central compressed gas passes out through the colder surrounding pusher. They can be used to determine both the temperature and the $\rho\Delta R$ product of the pusher around peak compression. Fair agreement is found between the experimental absorption spectra and simulations calculated by a hydrodynamic code. Applications of this work to the diagnosis of future, high-compression implosions is discussed.

I. INTRODUCTION

The use of emission spectroscopy for diagnosis of conditions in the compressed gas core of laser-imploded targets has received considerable attention.[1] Another important problem is the characterization of the pusher shell containing the fill gas. The temperature in the pusher is often too low ($\lesssim 100$ eV) for self-emission to be useful as a diagnostic. This is because to probe such low temperatures we would need to detect lines of low-Z species. However, these low-energy lines will be heavily absorbed by photoionization in a sufficiently dense or thick tamper, thereby preventing such a measurement. As an alternative we have investigated the use of absorption spectroscopy in pusher characterization. Experiments were performed with CO_2-laser-imploded targets which demonstrate the utility of this technique for future laser fusion experiments.

High temperatures ($\gtrsim 1$ keV) are often obtained in the central gas core of laser-imploded targets. Under these conditions, the continuous x-ray emission from the core passes out through the pusher and undergoes absorption at wavelengths characteristic of atomic species in the tamper. A schematic diagram illustrating this effect is shown in Fig. 1. The resulting absorption lines can yield information on the temperature (T_e), density (ρ), and the $\rho\Delta R$ product (density times thickness) of the tamper.

Particularly, strong absorption can be caused by resonance line transitions of the type $1s$-$2p$ in ions which have one or more vacancies in the $n=2$ shell; these are thus inner-shell transitions. The optimal choice of tamper species for this method is such that at the prevailing tamper temperature, ionization will remove some of the L-shell ($n=2$) electrons, as well as all electrons of higher shells. For the present experiment, potassium and chlorine bracketed the range of anticipated temperatures, and therefore a KCl absorption layer was embedded within the tamper. Chlorine and potassium absorption lines were indeed observed and used to determine the conditions within the KCl layer, and by inference, within the rest of the tamper.

The method of using pusher (tamper) absorption lines was previously reported by Yaakobi *et al.*[2] at the Laboratory for Laser Energetics (LLE) and by Hauer[3] and collaborators at Los Alamos National Laboratory. Bradley, Hares, and Kilkenny at Rutherford Appleton Laboratory reported on similar observations in planar targets. We discuss below the advantage of using absorption by higher-Z ions and analyze the results in more detail than has been previously done. The values of T_e and $\rho\Delta R$ derived from the experiment are in fair agreement with those predicted by the LASNEX laser-fusion code.

Absorption spectroscopy provides the same information as the neutron-activation technique[5] (such as that using ^{28}Si), namely the $\rho\Delta R$ product of the target pusher. Absorption spectroscopy, can, however, provide more detailed information on density and ρR. In addition, it can be used for temperature measurements. The method can be further enhanced by time resolving the spectra. Furthermore, the method can also be extended to the backlighting mode, by using an external continuum source. In this case, the parameters of the fuel can also be determined if a high-Z dopant is used. More importantly, the method

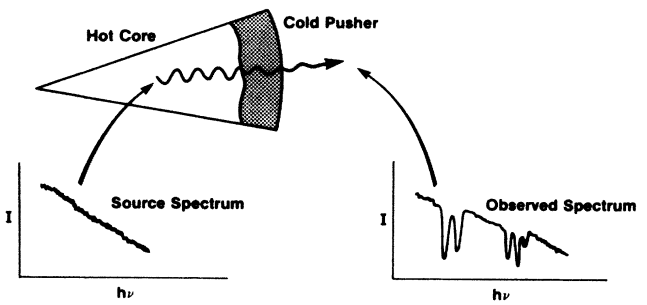

FIG. 1. Schematic representation of the measurement of cold-pusher parameters through the observation of absorption lines in a continuum emitted by the hot compressed core.

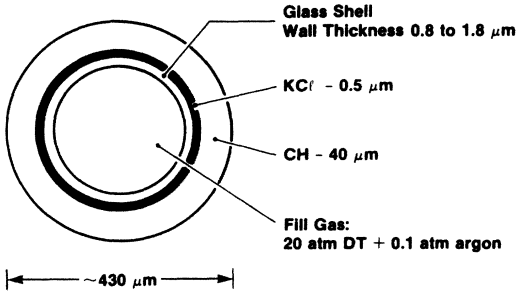

FIG. 2. Typical target parameters used in this experiment.

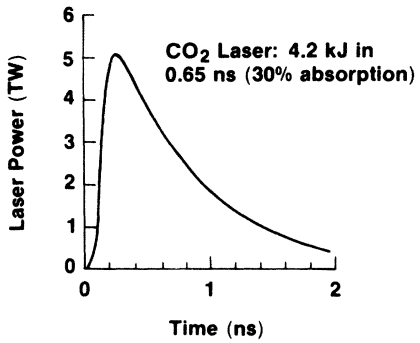

FIG. 3. Typical laser parameters used in this experiment.

can then be applied even if the core is too cold to strongly emit x-ray continuum radiation.

II. EXPERIMENT

A typical target used in the present experiment is illustrated in Fig. 2. It consisted of a 350 μm diameter glass shell of thickness varying between 0.8 and 1.5 μm, coated with a 0.5 μm layer of KCl and then a 40 μm layer of $(CH)_x$. The fill gas was 15 atm of DT and 0.2-atm argon (a fraction of about 0.10 argon by mass or total number of electrons). The potentially severe electron preheat is mitigated by choosing a very thick tamper, leading to a modest preheat temperature. The tamper, after decompression due to the preheat, recompresses to modest ρ and $\rho\Delta R$ values and it is then that very distinct absorption lines (of Cl and K) appear in the spectrum. The argon doping causes a relatively small perturbation on the target behavior, but provides a signature for gas-core temperature diagnosis. In addition, it contributes to the continuum intensity in the range 2.5–3.5 keV, which is required for observing Cl and K absorption lines. The targets used in this study were imploded with the 8-beam Helios CO_2-laser system at the Los Alamos National Laboratory. The total laser energy was about 4.5 kJ in a pulse with a full width at half maximum (FWHM) of about 650 ps. In Fig. 3 the laser pulse shape is shown. Each of the eight beams were focused about 300 μm beyond the center of the target, giving relatively uniform illumination across the surface of the sphere.

With CO_2 laser irradiation, essentially all of the absorbed laser energy goes into a hot-electron distribution. The temperature of this distribution, as indicated by the slope of the hard x-ray continuum, was about 120 keV. The term "hot-electron temperature" in this paper refers to the slope of the x-ray spectrum rather than to the electron source temperature which is considerably higher. The implosion is thus driven by hot electrons.

The hot-electron drive has the characteristic of a high degree of smoothing, and relatively uniform drive is produced even when there are inhomogeneities in the laser beam profiles. The thick plastic shell limits the core

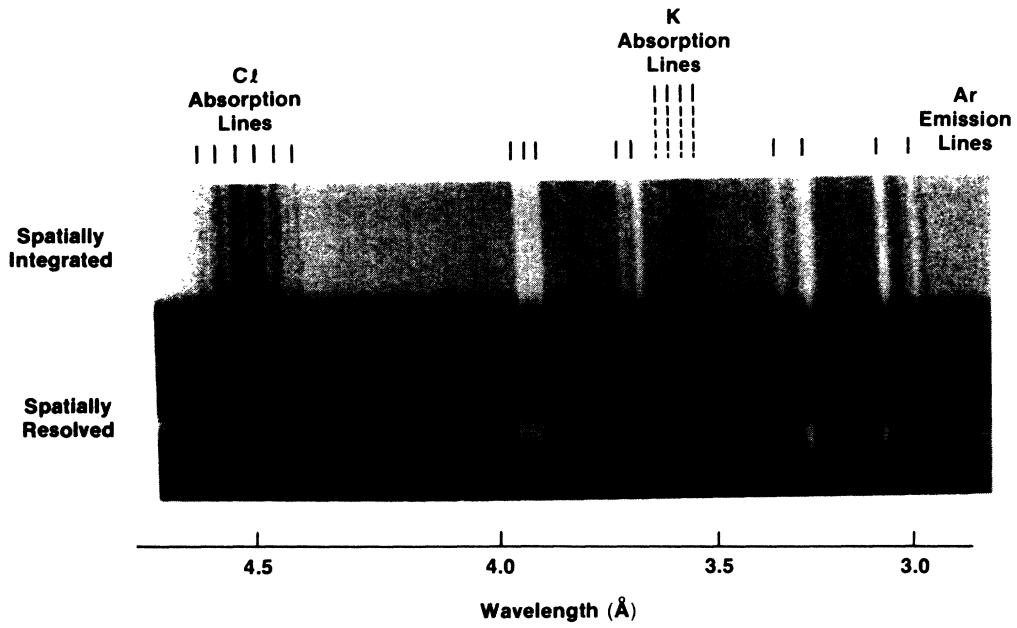

FIG. 4. Spatially integrated and spatially resolved spectrum emitted by the target in Fig. 2. Argon emission lines are due to Ar^{+16} and Ar^{+17} transitions. Chlorine and potassium absorption lines are due to $1s$-$2p$ transitions in ions with successive numbers of vacancies in the L shell.

preheat. The imploded gas core reaches electron temperatures of about 700 eV, which excites a strong continuum around 3 keV (as well as 3—4 keV argon lines), which is a prerequisite for observing chlorine absorption lines. The relative position of the embedded KCl layer within the target is such that by the time of peak compression, most or all of the $(CH)_x$ layer (but none of the KCl layer) has been ablated.

Figure 4 shows an example of the spectra emitted by these imploded targets. The spectra were recorded on film in both spatially integrated and spatially resolved mode (using a slit to obtain the spatial resolution). The spectrum was dispersed using a convex pentaerythritol (PET) diffracting crystal. The spatially-resolving slit was too wide to show detailed structure of the core, but performed the important function of confirming that the continuum giving rise to the absorption lines was emitted in a compressed core, i.e., near peak compression.

Figure 5 shows a microdensitometer trace of the spatially resolved portion of the spectrum in Fig. 4. There are two recombination continua: one (below about 5 Å) due to recombination of Si^{+14} ions, the other (below about 3.2 Å) due to recombination of Ar^{+17} ions. The slope of either of these continua corresponds to a temperature of about 700 eV. The argon line-intensity ratio $I(1s\text{-}2p)/I(1s^2\text{-}1s3p)$ can also be used to estimate the core temperature and it yields ~600 eV; this ratio is chosen to avoid the large opacity of the $1s^2\text{-}1s\,2p$ line. The contrast between strong-Ar emission lines and strong-Cl absorption lines vividly demonstrates a hot compressed core surrounded by a cooler shell. The tamper temperature deduced below is in fact much lower than this core temperature. The potassium lines appear less distinct than the chlorine lines, mainly because they are produced by a weaker continuum, and are, therefore, not analyzed in detail here. However, the absorption fractions on these lines and, therefore, the deduced $\rho\,\Delta R$ value are comparable to those of the chlorine lines.

Further information can be obtained from the spatially resolved portion of the spectrum. This trace eliminates some spurious radiation that is present in the spatially integrated spectrum and gives a more accurate judgment of the level of absorption. The background level lies just below the deepest absorption lines of Cl and K. This means that at the frequencies of peak absorption, the radiation emitted by the core goes through an optical depth that is significantly larger than 1.

III. ANALYSIS

Figure 6 shows in more detail the chlorine absorption structure. The identification of these line complexes was made by comparison with Hartree-Fock atomic structure calculations.[6] Table I summarizes the results of these calculations. As an example, the line marked *B* in Fig. 6 corresponds to transitions of the type $1s\text{-}2p$ in boronlike chlorine (Cl^{+12}), i.e., $1s^2 2s^2 2p\text{-}1s\,2s^2 2p^2$; we likewise refer to other lines as the Be or the C feature, etc. For each configuration there can be several atomic states. For example, the He and Be features contain only one transition (ignoring a second, spin-forbidden transition) whereas the B feature includes 14 transitions of which six are strong (i.e., for which gf is larger than 0.1); the C feature contains 35 transitions of which 12 are strong. The broadening of the B,C, and especially the N,O features is to a large extent due to the splitting between the lines comprising each manifold (which are blended because of additional broadening). For example, the measured width of the B feature is about 14 eV, that of the Be feature 17 eV. The widths due to line splitting of say, the B and N features are 6 and 12 eV, respectively. The Be feature has no such broadening. The wavelength ranges covered by lines belonging to a single charge state are shown in Fig. 7. Only the strong lines (for which $gf > 0.1$) were included in this representation.

The remaining broadening mechanisms affecting these features are instrumental (about 3 eV) and Stark broadening. Additionally, the results below indicate that the optical depth at the peak of the Stark profile for these lines is much greater than 1 (the FWHM of the central portion of the Stark profile of these lines is estimated to be less than 1 eV for an electron density of order $10^{23}\,cm^{-3}$). Under these conditions the core radiation at the peak of the profile is depleted. The absorption line then broadens to a

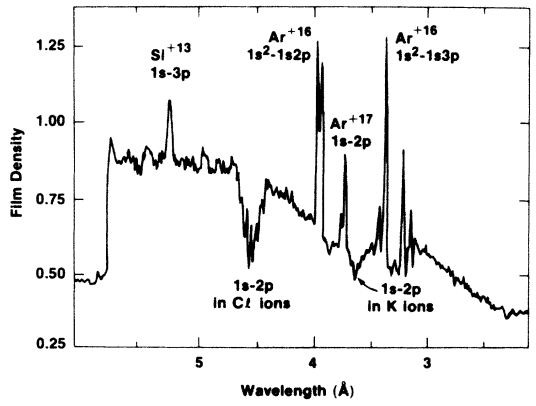

FIG. 5. Microdensitometer trace of the spatially resolved spectrum of Fig. 4.

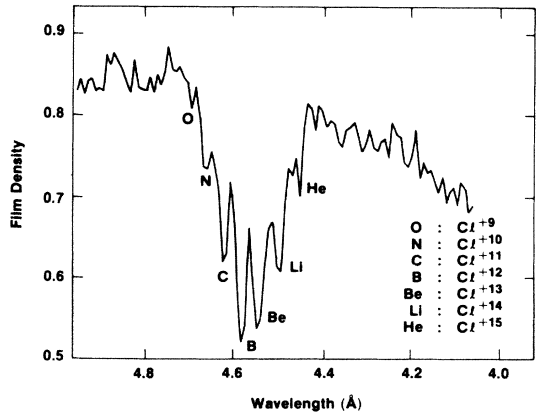

FIG. 6. Detailed tracing of the chlorine absorption lines of Fig. 4. The feature marked B corresponds to the transition $1s\text{-}2p$ in boronlike chlorine (Cl^{+12}), etc.

TABLE I. Transitions of the type $1s$-$2p$ in Cl ions. Only the strong transitions are included, for which $gf > 0.1$. The total number of transitions of this type is indicated for each ion.

Ground			Excited			
E (eV)	J	Conf.	J	Conf.	λ(Å)	gf
		Cl XVI (He-like), $1s^2$-$1s\,2p$ (2 transitions)				
0	0	$(^1S)^1S$	1	$(^1S)^1P$	4.4425	0.7890
		Cl XV (Li-like), $1s^2 2s$-$1s\,2s\,2p$ (6 transitions)				
0	$\frac{1}{2}$	$(^1S)^2S$	$\frac{1}{2}$	$(^1S)^2P$	4.4830	0.4213
0	$\frac{1}{2}$	$(^1S)^2S$	$\frac{3}{2}$	$(^3S)^2P$	4.4808	0.9582
		Cl XIV (Be-like), $1s^2 2s^2$-$1s\,2s^2 2p$ (2 transitions)				
0	0	$(^1S)^1S$	1	$(^2S)^1P$	4.5158	0.7369
		Cl XIII (B-like), $1s^2 2s^2 2p$-$1s\,2s^2 2p^2$ (14 transitions)				
0.7316	$\frac{3}{2}$	$(^1S)^2P$	$\frac{5}{2}$	$(^1D)^2D$	4.5638	0.7108
−1.4632	$\frac{1}{2}$	$(^1S)^2P$	$\frac{3}{2}$	$(^1D)^2D$	4.5608	0.5442
0.7316	$\frac{3}{2}$	$(^1S)^2P$	$\frac{1}{2}$	$(^3P)^2P$	4.5607	0.1857
−1.4632	$\frac{1}{2}$	$(^1S)^2P$	$\frac{1}{2}$	$(^3P)^2P$	4.5570	0.5228
0.7316	$\frac{3}{2}$	$(^1S)^2P$	$\frac{3}{2}$	$(^3P)^2P$	4.5569	1.2748
0.7316	$\frac{3}{2}$	$(^1S)^2P$	$\frac{1}{2}$	$(^1S)^2S$	4.5434	0.2136
		Cl XII (C-like), $1s^2 2s^2 2p^2$-$1s\,2s^2 2p^3$ (35 transitions)				
−3.1942	2	$(^3P)^3P$	3	$(^2D)^3D$	4.6056	0.7901
15.1642	0	$(^1S)^1S$	1	$(^2P)^1P$	4.6050	0.4576
3.8803	2	$(^1D)^1D$	2	$(^2P)^3P$	4.6046	0.1317
−4.4307	1	$(^3P)^3P$	2	$(^2D)^3D$	4.6039	0.5083
−5.3024	0	$(^3P)^3P$	1	$(^2D)^3D$	4.6025	0.2512
3.8803	2	$(^1D)^1D$	2	$(^2D)^1D$	4.5986	1.5712
−3.1942	2	$(^3P)^3P$	1	$(^4S)^3S$	4.5985	0.5664
−4.4307	1	$(^3P)^3P$	1	$(^4S)^3S$	4.5964	0.5728
−5.3024	0	$(^3P)^3P$	1	$(^4S)^3S$	4.5950	0.1775
−3.1942	2	$(^3P)^3P$	2	$(^2P)^3P$	4.5925	0.5281
−3.1942	2	$(^3P)^3P$	1	$(^2P)^3P$	4.5918	0.3400
3.8803	2	$(^1D)^1D$	1	$(^2P)^1P$	4.5858	0.5781

width such that the optical depth on the wings (e.g., the half-intensity points) is of order 1. This point is further discussed below. The line widths then depend on ρ and $\rho\,\Delta R$, and, because of the unavailability of Stark profile calculations for these lines, they are not used here as diagnostic signatures. When these become available, however, further analysis of the profiles could give very useful information on these imploded plasma parameters.

The tamper temperature at the time of strong continuum emission from the core can be inferred from the intensity ratios of the absorption features. At higher tamper temperatures than here, features like He or Li would dominate the absorption spectrum; at lower tamper temperatures it would be features like N and O. The fact that the absorption features have a sharply peaked distribution of intensity is an indication that they are formed over a period of time when the tamper temperature does not vary appreciably.

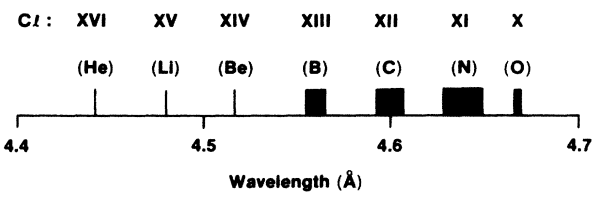

FIG. 7. Schematic representation of the wavelength interval over which the strong lines of chlorine ions extend. Strong line is defined here as having $gf > 0.1$, g is the lower-level statistical weight and f the absorption oscillator strength. The ion marked B is boronlike, or Cl XIII (Cl^{+12}), etc.

In order to estimate the tamper temperature from Fig. 6 we calculate the non-LTE steady-state distribution of chlorine charge states in a model which includes radiative, dielectronic and three-body recombination, as well as ionization (collisional-radiative equilibrium model). The results (Fig. 8) show that this distribution depends primarily on the temperature and only slightly on the density in the range $(1-10)\times 10^{23}$ cm^{-3}. For this density range the deduced temperature by comparison to Fig. 6 is in the range 200—230 eV. The width of the experimental and calculated distributions are comparable, indicating a temperature which does not vary appreciably over the time when the absorption features are formed. The determination of the tamper temperature in this case is, therefore, not degraded

TABLE I. (*Continued*).

Ground			Excited			
E (eV)	J	Conf.	J	Conf.	λ(Å)	gf
		Cl XI (N-like), $1s^2 2s^2 2p^3$-$1s\,2s^2 2p^4$ (35 transitions)				
7.5989	$\frac{3}{2}$	$(^2P)^2P$	$\frac{5}{2}$	$(^1D)^2D$	4.6482	0.3776
7.5989	$\frac{3}{2}$	$(^2P)^2P$	$\frac{3}{2}$	$(^3P)^2P$	4.6439	0.3689
7.2399	$\frac{1}{2}$	$(^2P)^2P$	$\frac{3}{2}$	$(^3P)^2P$	4.6433	0.2160
7.5989	$\frac{3}{2}$	$(^2P)^2P$	$\frac{1}{2}$	$(^3P)^2P$	4.6423	0.1381
7.2399	$\frac{1}{2}$	$(^2P)^2P$	$\frac{1}{2}$	$(^3P)^2P$	4.6416	0.2769
−10.9511	$\frac{3}{2}$	$(^4S)^4S$	$\frac{5}{2}$	$(^3P)^4P$	4.6394	0.6615
−10.9511	$\frac{3}{2}$	$(^4S)^4S$	$\frac{3}{2}$	$(^3P)^4P$	4.6371	0.4435
−10.9511	$\frac{3}{2}$	$(^4S)^4S$	$\frac{1}{2}$	$(^3P)^4P$	4.6359	0.2221
−0.2677	$\frac{3}{2}$	$(^2D)^2D$	$\frac{3}{2}$	$(^1D)^2D$	4.6353	0.8252
0	$\frac{5}{2}$	$(^2D)^2D$	$\frac{5}{2}$	$(^1D)^2D$	4.6350	0.9247
0	$\frac{5}{2}$	$(^2D)^2D$	$\frac{3}{2}$	$(^3P)^2P$	4.6307	1.0498
−0.2677	$\frac{3}{2}$	$(^2D)^2D$	$\frac{1}{2}$	$(^3P)^2P$	4.6286	0.4598
7.5989	$\frac{3}{2}$	$(^2P)^2P$	$\frac{1}{2}$	$(^1S)^2S$	4.6282	0.3621
		Cl X (O-like), $1s^2 2s^2 2p^4$-$1s\,2s^2 2p^5$ (14 transitions)				
14.139	0	$(^1S)^1S$	1	$(^2S)^1P$	4.6867	0.2119
−2.897	1	$(^3P)^3P$	2	$(^2S)^3P$	4.6751	0.2655
−2.473	0	$(^3P)^3P$	1	$(^2S)^3P$	4.6735	0.2125
−4.185	2	$(^3P)^3P$	2	$(^2S)^3P$	4.6728	0.7874
−2.897	1	$(^3P)^3P$	1	$(^2S)^3P$	4.6727	0.1574
−2.897	1	$(^3P)^3P$	0	$(^2S)^3P$	4.6712	0.2126
−4.185	2	$(^3P)^3P$	1	$(^2S)^3P$	4.6704	0.2724
3.587	2	$(^1D)^1D$	1	$(^2S)^1P$	4.6681	1.0506

as a result of not resolving the spectrum in time. Time resolution could, however, be useful in determining when the absorption occurs and studying the onset of absorption as a function of varying implosion conditions.

The determination of the tamper $\rho\,\Delta R$ from the absorption lines is based on the cross section for photo absorption on a spectral line of profile $\phi(\nu)$, normalized to total area of unity

$$\sigma_\nu=(\pi e^2/mc)f\phi(\nu)=\sigma_0\phi(\nu)\ , \tag{1}$$

where f is the absorption oscillator strength.

The attenuated intensity $I(\nu)$ through a layer of thickness ΔR and density ρ is related to the incident intensity I_0 (assumed independent of frequency) through

$$I(\nu)=I_0\exp(-\sigma_\nu N_p\,\Delta R)=I_0\exp(-\sigma_\nu\alpha\rho\,\Delta R/M_i)\ , \tag{2}$$

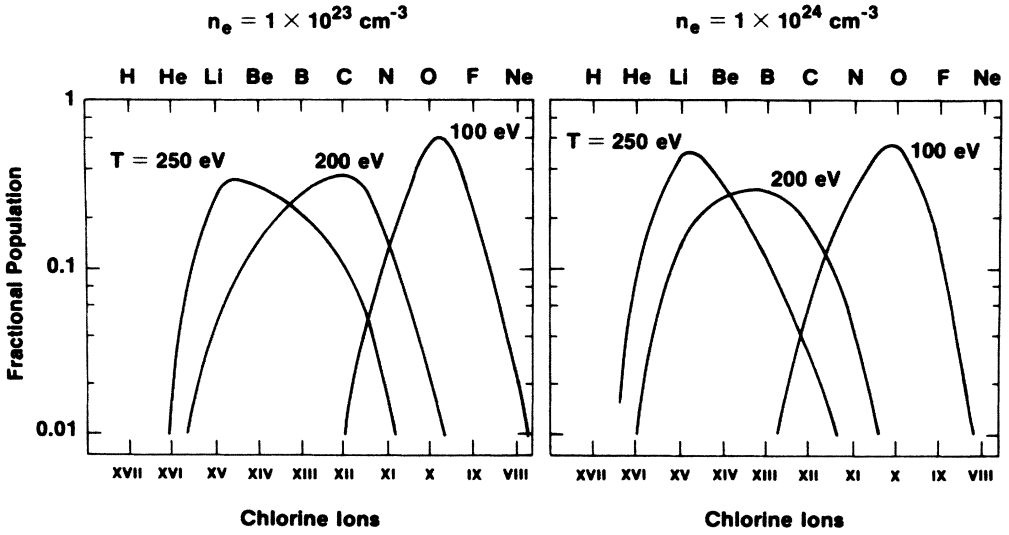

FIG. 8. Atomic model calculations of chlorine charge-state distribution at two densities. Smooth lines connect the calculated discrete points. Comparison of such curves to the spectrum of Fig. 6 is used to estimate the tamper temperature.

where α is the fraction of all ions of ionization state p, whose density is N_p, which are in the ground state. For the case of absorption lines α is inevitably very nearly equal to 1, because the temperature where they are formed is much smaller than the excitation energy of these lines. For some of these chlorine ions the ground configuration consists of several closely spaced states and their total population densities are added; this means that the f value in Eq. (1) has to be averaged over the lower-state levels as well as summed over the upper-state levels. As examples, the Be ion has one ground state ($^1S_0$), the B ions two ($^2P_{1/2}, ^2P_{3/2}$), and the C ion five ($^1D_2, ^1S_0, ^3P_2, ^3P_1, ^3P_0$).

The $\rho\Delta R$ can then be derived from the equation

$$\rho\Delta R = (M_i/\sigma_0\alpha)\int \ln(I_0/I_\nu)d\nu \ . \tag{3}$$

The integral is effectively over the line profile because the integrand vanishes far from line center. In the approximation that the film density in Fig. 5 is exactly proportional to $\ln(I)$, this integral is simply the area enclosed within the absorption line. For each absorption line this equation yields the partial $\rho\Delta R$ value related to the corresponding ion. The total $\rho\Delta R$ of the KCl layer is given by

$$\begin{aligned}\rho\Delta R(\mathrm{KCl}) &= \rho\Delta R(\mathrm{K}) + \rho\Delta R(\mathrm{Cl}) \\ &= 2.1\rho\Delta R(\mathrm{Cl}) = 2.1\sum_p \rho\Delta R(\mathrm{Cl}_p) \ ,\end{aligned} \tag{4}$$

where the summation is over the absorption line manifold such as that shown in Fig. 6.

It is important to note that only the integral over the line profile is required for the determination of $\rho\Delta R$, so that the line profile need not be known.[7] Also, the deconvolution required to separate the contribution of the partly overlapping absorption lines is not critical. For example, if the f values of these absorption lines were the same, we would only need to integrate the entire absorption manifold of Fig. 6, without any deconvolution.

Applying the procedure described here to the absorption lines of Fig. 6, following conversion from film density to intensity, overlapping lines deconvolution and integration, we derive a value of $\rho\Delta R = 5.1\times10^{-4}$ g/cm^2 for the KCl layer. The main sources of error in deriving the $\rho\Delta R$ value come from the determination of the area enclosed within the absorption lines, and from uncertainties in film calibration curves. These errors are estimated to be $\pm 20\%$. An additional error in time-integrated spectra can be caused by core emission of continuum, prior to the time when the absorption lines are formed. This can occur when the core starts to compress and heat up, but the shell still moves inwards and is too cold to absorb on $1s$-$2p$ transitions, because there are no vacancies in the $n=2$ electronic shell. This error should in general be small because of the logarithmic dependence of the derived $\rho\Delta R$ value on the measured intensity [Eq. (3)]; it always results in underestimating the correct $\rho\Delta R$ value. If at least one of the absorption lines approaches the background level (as is the case for both the Cl and K groups in Fig. 5), then this effect is unimportant.

We used the LASNEX laser-fusion code in a one-dimensional mode to simulate these experiments. The simulations were very similar to those described in Ref. 8, which gives further details on the hydrodynamic and spectral modeling tools employed here. The target and laser conditions used in the examples in Ref. 8 are, however, somewhat different than in the present experiment. Typical simulation results of the temporal behavior of target parameters are shown in Figs. 9–11. The time scale in these figures is the same as in Fig. 3; the latter shows that the laser pulse rises fast to its peak at 0.3 ns and falls to half its maximum value at 0.8 ns. In Fig. 9 we show the time history of the electron temperature, averaged separately over each target layer. At the time of peak core temperature, which should be about the time of peak core emission of continuum, the temperature in the KCl layer is 250 eV, in good agreement with the range 200–230 eV determined from the experiment. It should be pointed out that the predicted preheat temperature is only about 80 eV. The rise in tamper temperature at about 1.1 ns is due to heat flowing outwards from the hot fill gas as well as due to the recompression of the expanded tamper. In Fig. 10 the predicted variation of mass density as a function of time is shown. As is evident from Fig. 10, the compression occurs much after the peak of the laser pulse. Direct hot-electron pumping of excited states is thus not a factor in the present analysis. The hot-electron temperature used in the simulation was chosen to be consistent with hard x-ray bremsstrahlung measurements. Modest variations in this value did not result in significant charges in the implosion characteristics.

Figure 11 shows the time history of the $\rho\Delta R$ of both the glass and KCl layers. We assume that line formation occurs near the time of peak emission. This interval should be roughly between peak temperature and peak density.[8] This assumption is corroborated by information from simulations described below. At the time of peak emission, the $\rho\Delta R$ of the KCl layer is about 10^{-3} g/cm^2, which is about twice the experimentally derived value. The sources of this difference between theory and experiment include (a) inaccuracy in the measurement of the background and continuum levels; (b) error due to time integration effects; and (c) error in the simulation itself, such as the hot-electron-transport methods.

Future measurements of such spectra will be made with time resolution which should give more accurate results.

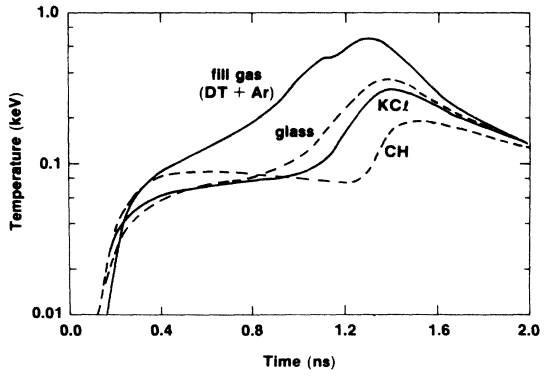

FIG. 9. LASNEX-calculated temperature history for the experiment of Fig. 4, averaged over each of the four target layers. Time scale (here and in Figs. 10 and 11) is the same as in Fig. 3.

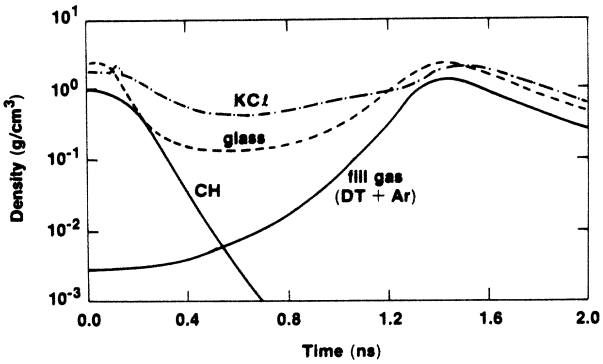

FIG. 10. LASNEX-calculated density history, averaged over each of the four target layers.

We can infer from this by using the computational results of Fig. 11 that the total $\rho\Delta R$ of the tamper at the time of peak emission was about 3.2×10^{-3} g/cm^2. An important conclusion from Figs. 9—11 is that for the present method to be most useful the peak in core emission should occur at about the same time as the peak in the tamper $\rho\Delta R$.

Another indication of the accuracy of the simulation is obtained from the compressed gas-core conditions. The argon-line profiles give an average compressed core electron density of about 3×10^{23} cm^{-3}, in agreement with simulation. In addition, the spatially-resolved spectra and x-ray pinhole photographs are consistent with the spatial distribution of x-ray emission predicted by the simulation.

In order to directly simulate the absorption spectra, multigroup opacity tables were generated using the OPLIB opacity library (explained in Ref. 9). The atomic structure and cross-section calculations used in OPLIB generated the absorption data corresponding to all of the inner-shell transitions observed in the absorption spectra. The resulting opacity tables were then used on line, as part of the LASNEX simulation. The use of the OPLIB opacity calculations requires the assumption of LTE conditions. For the high-density, low-temperature conditions that prevail in the tamper this is a fair approximation. It should be emphasized that the assumption of LTE is not critical when calculating absorption lines. Whereas emission lines depend on the population of excited levels which can vary greatly between LTE and non-LTE model predictions, absorption lines depend on ground-state populations which are essentially equal to the total density of the pertinent ion species. The LTE assumption in the absorption region does have an effect in determining the partition of the ion populations among the various ion species. Deviations from LTE would only shift the calculated distribution among the absorption lines, but will hardly affect the total absorption enclosed within the absorption lines (small changes in the latter will occur because the f values for the various absorption lines are not identical). We show in Fig. 12 an example of the absorption-coefficient data calculated by OPLIB for a particular set of temperature and density. In addition to the transitions of the type $1s$-$2p$, the absorption data also include $1s$-$3p$ transitions which are, however, too weak to appear distinctly in the experimental spectra. The opacity is given by the product of the absorption coefficient and the $\rho\Delta R$ value for the corresponding atomic specie. By multiplying the $\rho\Delta R$ values for individual chlorine ions as obtained here, by the absorption coefficient from Fig. 12, we obtain peak opacity values of order 1. This may seem to be at odds with the claim made earlier that the opacity on the peak of the strong chlorine absorption lines is much higher than 1. However, the absorption-coefficient values in Fig. 12 depend on the energy resolution chosen in calculating them. If the energy intervals are coarse, this is equivalent to assuming large line widths, which will result in lower opacity. The choice of energy resolution will not materially change the area under the absorption features or their intensity ratios. For the present calculation we chose energy intervals which are about equal to the measured line width. In this way we account directly for the instrumental broadening (rather than first calculating narrow absorption profile and then account for their additional opacity and instrumental broadening).

In Fig. 13 we show the results of the spectral simulation corresponding to the specific implosion that pro-

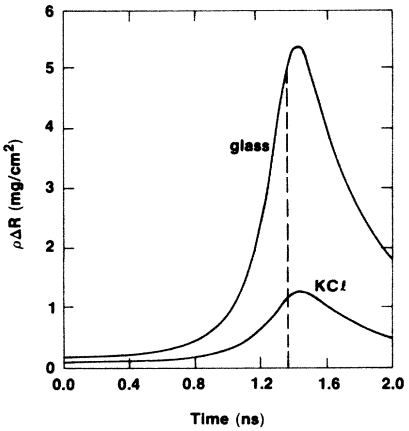

FIG. 11. LASNEX-calculated $\rho\Delta R$ history for the two tamper layers. The vertical line shows the time around which the absorption lines are mostly formed.

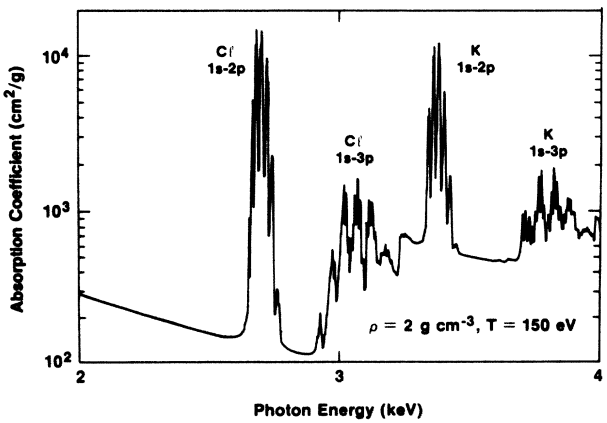

FIG. 12. Sample KCl data from the OPLIB opacity tables for a set of temperature and density values. Such data were used in LASNEX runs to obtain the simulated spectrum of Fig. 13.

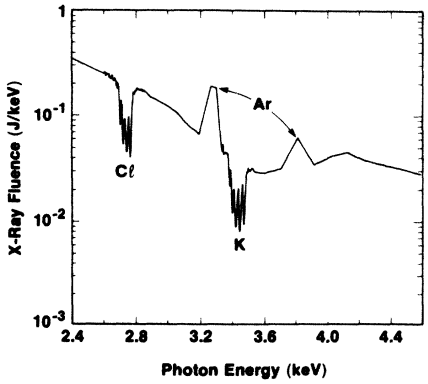

FIG. 13. LASNEX-calculated, time-integrated x-ray spectrum emitted from the target, simulating the experiment of Fig. 4.

duced the spectrum in Fig. 4. OPLIB opacities were used only for the KCl layer. Argon emission was calculated with the average ion non-LTE opacity routine in LASNEX.[10] Fine spectral resolution was used in the regions around the chlorine and potassium features and coarse resolution elsewhere. The feature around 3.8 keV is due to the non-LTE calculation of argon emission. The depth of the absorption features in the simulation is similar to that observed in the experimental spectrum. The distribution of charge states in the simulation is somewhat different than in the experiment. This is due partly to the slightly higher tempertaure in the simulation (250 eV as compared with 200—230 eV). The higher temperature in the simulation is also accompanied by a higher core temperature than in the experiment and thus a smaller continuum slope. Figure 8 provides an indication of significant change in the distribution of absorption line intensities when the temperature changes from, say, 200 to 250 eV. Additionally, the LTE assumption in OPLIB increases the ionization to higher charge states than predicted by a non-LTE model for the same temperature. It should be emphasized that the derivation of pusher temperature proceeds by comparing the measured spectrum to the non-LTE curves of Fig. 8, without reference to a hydrodynamic code. The LASNEX results are shown in order to demonstrate the ability to replicate the very existence of absorption lines in the spectrum. This satisfying result shows an overall correct code description of target behavior. Furthermore, whereas the LTE assumption in OPLIB causes a shift to higher ionization in the distribution of absorption lines, the total absorption in the group of Cl or K lines should essentially still be correctly predicted; this is indeed approximately the case (comparison of Figs. 13 and 5).

Although time resolution was not available in the present experiment, the simulation gives an indication of the information that would be available from time-resolved data. Figure 14 shows the simulated chlorine absorption features, time integrated up to several time instances during the implosion. This gives a good indication of the dynamic range that would be necessary in a time-resolving instrument (such as a streak camera) in order to observe the absorption data at times far from peak

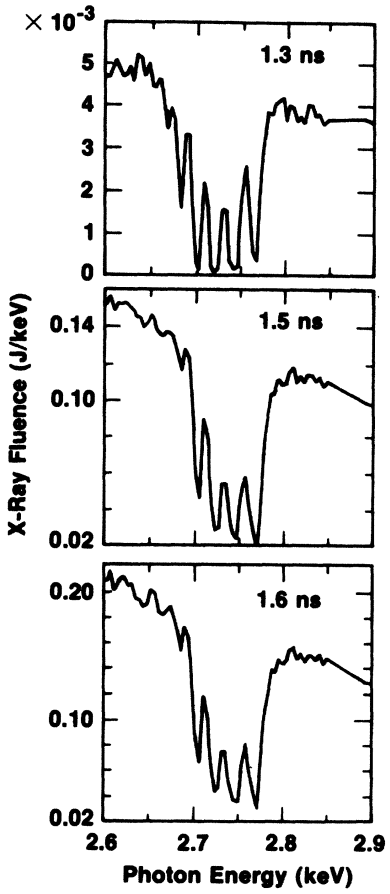

FIG. 14. LASNEX-calculated spectrum of chlorine absorption lines, integrated up to the time marked for each figure.

$\rho\Delta R$. The results show that absorption lines are formed mainly during a short time interval (1.4—1.5 ns) and therefore time-integrated results in this case give a snapshot of conditions during peak core continuum emission.

IV. CONCLUSIONS AND SUGGESTIONS FOR FUTURE WORK

We have shown in this experiment and its analysis that absorption spectroscopy can be used to provide important diagnostic information on the conditions of the tamper in laser-implosion experiments. Penetrating high-energy radiation was thus used to diagnose low-temperature imploded material whose self-emission could not be observed. For the $\rho\Delta R$ values reached in the pusher, the self-emission at a temperature of about 200 eV would be soft enough, so that only radiation from a thin outer layer would escape the pusher. This is why diagnosis of the pusher has to make use of absorption-line techniques.

A direct extension of the present work to future high-performance target implosions (such as those expected with short-wavelength lasers) might require that a very thin absorbing signature layer be placed in a low-Z plastic shell. This is because a high $\rho\Delta R$ compressed shell can absorb strongly even photons of nonresonant frequency

(by the photo-electric, or bound-free mechanism) so that no absorption lines would appear in the spectrum. This problem will be especially severe in such targets because the tamper temperature is expected to be lower, which will necessitate choosing a lower-Z signature layer, or no electrons of the $n=2$ shell will be ionized. Lower-Z ions have transitions of longer wavelength where the absorption is even more severe. To counter such excessive absorption the targets should have a thin enough signature layer, located deep enough in a low-Z tamper, so that it does not undergo ablation or expansion before peak compression of the core. The choice of chlorine for the present experiment was appropriate because for higher Z (even for potassium) the continuum intensity becomes weaker and this limits the precision of the measurement; on the other hand, for much lower Z, the glass shell absorption is severe even in the present experiment. A more detailed determination of tamper parameters can be obtained by embedding several signature layers within the inner part of the tamper, with deeper layers having a higher nuclear charge Z.

As an indication of the effects encountered in higher-density (and lower preheat) compressions, we performed some simulations using a lower hot-electron temperature than was actually observed in these experiments. As an example, we show in Fig. 15 the predicted chlorine absorption spectrum for a hot-electron temperature of about 40 keV, compared with the case of $T_H=110$ keV from Fig. 13. The lower T_H reduces the preheat in both the gas and pusher, causing a shift in the distribution of absorption-line intensities towards lower charge states. This in turn results in a denser implosion which is evidenced by slightly deeper Cl absorption lines.

Another important question is the use of an external radiation source to perform absorption studies on both the tamper as well as the core of the target. This would allow for greater flexibility in choosing the spectrum, the timing, and other characteristics of the probing radiation. The difficulty here will be in arranging for a convenient source and spectrograph configuration. This will have to allow for sufficient spatial resolution to discriminate against radiation from the backlighting source which bypasses the compressed core, and thus contributes to a spurious background. Additionally, because a typical compressed core would subtend a very small angle at the backlighting source, the range of wavelengths going through the core would normally be very small (since wavelengths and angles are related through the Bragg condition). To overcome this, the distance between the main and auxiliary targets should be kept to a minimum and the diffracting crystal should be convexly bent to a small radius of curvature.

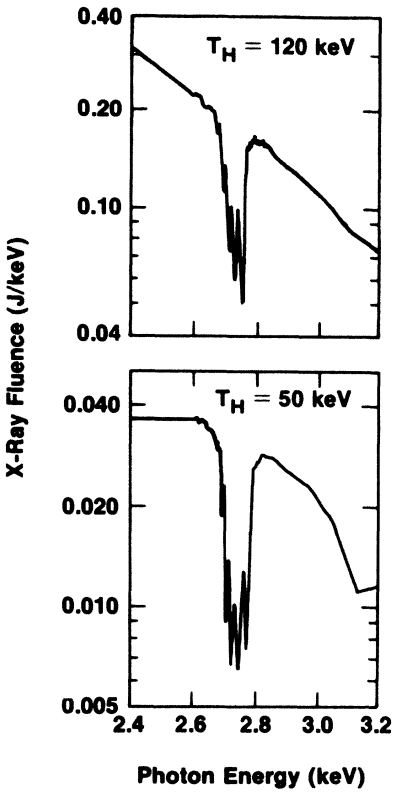

FIG. 15. Comparison of LASNEX-calculated, time-integrated spectrum of chlorine absorption lines for two values of the hot-electron temperature T_H: (a) 120 keV, from Fig. 13; (b) 50 keV, with all other parameters the same.

ACKNOWLEDGMENTS

Helpful discussions on the subject of absorption spectroscopy with Professor Hans Griem and with J. D. Kilkenny are gratefully acknowledged, as is the valuable help with the simulations from John Keady and John Norton. We wish to thank the Los Alamos HELIOS operations and target fabrication groups for invaluable work in the performance of these experiments. This work was supported by the U.S. Department of Energy Office of Inertial Fusion under Contract No. DE-FC08-85DP40200 and by the Laser Fusion Feasibility Project at the Laboratory for Laser Energetics which has the following sponsors: Empire State Electric Energy Research Corporation, General Electric Company, New York State Research and Development Authority, Ontario Hydro, Southern California Edison Company, and the University of Rochester.

[1]B. Yaakobi, S. Skupsky, R. L. McCrory, C. F. Hooper, H. Deckman, P. Bourke, and J. M. Soures, Philos. Trans. R. Soc. London Ser. A **300**, 623 (1981); A. Hauer, K. B. Mitchell, D. B. VanHulsteyn, T. H. Tan, E. J. Linnebur, M. M. Mueller, P. C. Kepple, and H. R. Griem, Phys. Rev. Lett. **45**, 1495 (1980); J. D. Kilkenny, R. W. Lee, M. H. Key, and J. G. Lunney, Phys. Rev. A **22**, 2746 (1980).

[2]B. Yaakobi, R. L. McCrory, S. Skupsky, J. A. Delettrez, P. Bourke, H. Deckman, C. F. Hooper, and J. M. Soures, Opt. Commun. **34**, 213 (1980).

[3]A. Hauer, in *Spectral Line Shapes*, edited by B. Wende (Springer, Berlin, 1981).

[4]D. K. Bradley, J. D. Hares, and J. D. Kilkenny, Rutherford Appleton Laboratory, Annual Report No. RL-83-043, 1983, p. 5.4 (unpublished).

[5]F. J. Mayer and W. B. Rensel, J. Appl. Phys. **47**, 1491 (1976); E. M. Campbell, W. M. Ploeger, P. H. Lee, and S. M. Lane, Appl. Phys. Lett. **36**, 965 (1980).

[6]R. D. Cowan, J. Opt. Soc. Am. **58**, 808 (1968). Also, R. D. Cowan, *The Theory of Atomic Structure and Spectra* (University of California Press, Berkeley, 1981).

[7]A. Mitchell and M. Zemansky, *Resonance Radiation and Excited Atoms* (MacMillan, New York, 1934), p. 96.

[8]A. Hauer, K. G. Whitney, P. C. Kepple, and J. Davis, Phys. Rev. A **28**, 963 (1983).

[9]The calculations used in constructing these tables are illustrated in M. F. Argo and W. Heubner, J. Quant. Spectrosc. Radiat. Transfer **16**, 1091 (1976).

[10]W. A. Locke and W. H. Grasburger, Lawrence Livermore National Laboratory, Report No. UCRL 52276, 1977 (unpublished).

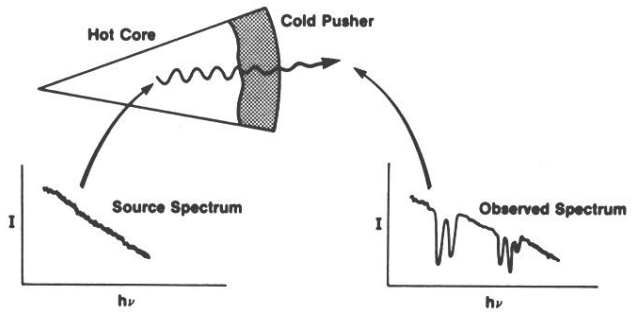

FIG. 1. Schematic representation of the measurement of cold-pusher parameters through the observation of absorption lines in a continuum emitted by the hot compressed core.

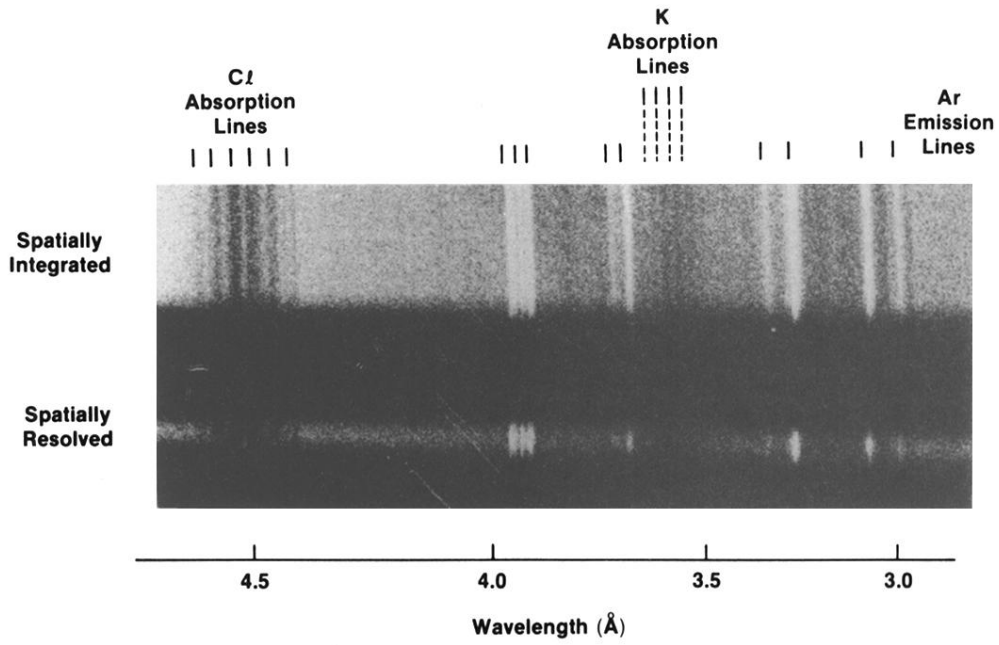

FIG. 4. Spatially integrated and spatially resolved spectrum emitted by the target in Fig. 2. Argon emission lines are due to Ar^{+16} and Ar^{+17} transitions. Chlorine and potassium absorption lines are due to $1s$-$2p$ transitions in ions with successive numbers of vacancies in the L shell.